

Atomistic Modelling of High-Entropy Layered Anodes and Their Electrolyte Interface

Amreen Bano* and Dan T Major

Department of Chemistry and Institute of Nanotechnology and Advanced Materials,
Bar-Ilan University, Ramat Gan, Israel-5290002

*Email: banoamreen.7@gmail.com

Abstract

Van der Waals (vdW) heterostructures have attracted intense interest worldwide as they offer several routes to design materials with novel features wide-ranging applications. Unfortunately, at present, vdW heterostructures are restricted to a small number of stackable layers, due to the weak vdW forces holding adjacent layers together. In this work, we report on computational studies of a bulk vdW material consisting of alternating TiS_2 and TiSe_2 (TSS) vertically arranged layers as a potential candidate for anode applications. We use density functional theory (DFT) calculations and ab-initio molecular dynamics (AIMD) simulations to explore the effect of high entropy on several electrochemically relevant properties of the bulk heterostructure (TSS-HS) by substituting Mo^{6+} and Al^{3+} at the transition metal site (Ti^{4+}). We also study the solvation shell formation at the electrode-electrolyte interface (EEI) using AIMD to determine Li-coordination. Based on the properties computed using DFT and AIMD we propose that high entropy TSS-HS (TSS-HE) might possess improved electrochemical performance over standard TSS-HS. Factors that could improve the performance of TSS-HE are 1) Less structural deformation, 2) Strong bonding (Metal-O), 3) Better electron mobility, 4) Higher theoretical specific capacity, 5) Wider operational voltage window, and 6) Faster Li-ion diffusion. Our observations suggests that ‘high entropy’ can be an effective strategy to design new anode materials for improving electrochemical performance of Li-ion batteries.

Introduction

Owing to their high energy density, low cost, large storage capacity and cycling stability, lithium-ion batteries (LIBs) have gained tremendous attention as electronic energy storage devices.¹⁻⁴ Since the discovery of graphene, with its high electroconductivity and specific surface area, graphene-based anode materials have been studied extensively.⁵ However, poor mechanical stability and low specific capacity⁶ are some limiting factors which are difficult to overcome, prompting researchers to look for improved or alternative anode materials. These strategies include doping,^{7, 8} strain,^{9, 10} defects,^{11, 12} or heterostructures with different layered materials.^{5, 13} In this regard, heterostructures are an attractive alternative that have already shown great promise. The distinct layers of heterostructures are held by interlayer van der Waals (vdW) interactions. These heterostructures not only exhibit new basic physics,^{14, 15} but also considerable performance in applications such as field-effect transistors^{13, 16, 17} and photodetectors.¹⁸⁻²⁰ Additionally, there is a plethora of literature focusing on the virtues of graphene-like heterostructures used as electrode materials.²¹⁻²³ Some promising post-graphene candidates are transition metal dichalcogenides (TMDs),²⁴⁻²⁷ phosphorene,²⁸ and silicene.²⁹ The layered TMD materials not only have properties similar to graphene, but they also have many mechanical, optical, chemical, thermal, and electrical capabilities that are comparable to or superior than graphene.^{27, 30, 31} The weak interlayer dispersion interactions in TMDs or their heterostructures facilitate intercalation of foreign atoms (such as Li-ions) which is reported to improve the electron conductivity of the material.³² Hence, layered TMDs and their heterostructures have previously been proposed as promising anode materials for LIBs.^{33, 34}

Commonly, a vdW heterostructure is prepared by mechanically stacking one two-dimensional (2D) layer on top of another. Interestingly, some bulk vdW heterostructures exist in nature, like Frankencite, which is a naturally occurring vdW heterostructure composed of SnS₂ and PbS layers stacked alternately.³⁵ There are few examples of such bulk vdW heterostructures, and synthesizing such heterostructures remains difficult despite the advancements in 2D materials research. Another example of a bulk vdW heterostructure is the 6R-phase of TaS₂, which consists of alternating layers of 1H-(superconducting)^{36, 37} and 1T-TaS₂ (Mott insulator)³⁸. Two typical layered TMD materials, TiS₂ and TiSe₂, have gained traction as potential anode materials.³⁹⁻⁴³

The performance of heterostructures as anode materials has been studied extensively for materials like MoS₂/WS₂,⁴⁴ WS₂/NbSe₂,⁴⁵ and NiSe₂/SnSe₂.⁴⁶ Still, to increase the choice of possible anode materials it is desirable to go beyond these base materials and pursue more complex materials. Considering the difficulty in synthesizing heterostructures it is of value to first consider potential materials in silico. Here we focus on the heterostructures with ‘high entropy’ elemental configuration. The study of high entropy battery materials commenced with the development of high entropy metal oxides as LIB anodes that showed significant improvement in specific capacity and capacity retention.⁴⁷⁻⁴⁹ This direction was further expanded to high entropy Li-ion cathodes that showed improved electrochemical performance.^{50, 51} We note that the terms ‘high entropy’,

‘compositionally complex’ and ‘multi-component’ are not necessarily interchangeable. Under ideal mixing conditions, where components are randomly distributed, the configurational entropy is expressed as:⁵²

$$S_{Config}^{Ideal} = -k_B \sum_{i=1}^N x_i \ln x_i \quad (1)$$

where x_i indicates the mole fraction of component i on the site of mixing. To be considered high entropy, a material must have an S_{Config}^{Ideal} value of $\geq 1.5R$.⁵³ For instance, the traditional cathode material $LiNi_{0.5}Mn_{0.3}Co_{0.2}O_2$, has an S_{Config}^{Ideal} of $1.03k_B$ per transition metal, and therefore cannot be considered a ‘high entropy’ material.⁵⁴ High-entropy materials can produce a large ensemble of local environments instead of the formation of local homogenous domains with clusters of like atoms which can form in low-entropy materials. Studies have indicated that multi-ensemble local environments might reduce the short-range ordering which is one of the causes of impaired electrochemical performance. Reduced short-range ordering enables ‘high entropy’ materials to attain higher rates and capacities.^{51, 55} In addition, compared to low-entropy materials, high-entropy materials show a greater tolerance for lattice distortions, allowing for significant changes to the energy landscape for ion diffusion.. As recently demonstrated in high-entropy oxide-based materials, carefully designed lattice distortions can produce percolating diffusion routes, allowing orders of magnitude increase in ionic conductivities.⁵⁶

In this work, we studied the effect of high entropy on structural, electronic, bond strength, and ion diffusion characteristics of a typical bulk heterostructure anode TSS-HS using DFT and AIMD calculations. Additionally, we explored Li-ion diffusion at the anode-electrolyte interface. Our analysis suggests that high entropy TSS-HS anode materials can improve overall electrochemical performance and warrant further experimental study.

Computational Methods

Using DFT, we performed high-throughput calculations on pristine and high entropy 1T-TiS₂-TiSe₂ (TSS) bulk heterostructure (HS) to explore its potential as a layered anode material for Li-ion batteries. To meet the ‘high entropy’ criteria, i.e., $N \geq 5$, we substitute Mo and Al at the transition metal site (Ti). Several Ti-substitution sites were explored using DFT to find suitable spots for Mo and Al in TSS-HS. Using *equation (1)*, we obtained $S_{Config}^{Ideal} = 1.44k_B$ per component for our TSS-HE anode model. The optimized TSS-HS and high-entropy TSS (TSS-HE) are shown in Fig. 1 (a, b). A supercell of $3 \times 3 \times 2$ was used to build the TSS-HS and TSS-HE models. All DFT calculations used the Vienna ab initio simulation package (VASP).^{57, 58} For all computations, projector augmented wave (PAW) potentials⁵⁹ were utilized. The electron-exchange correlation term was treated using the Perdew, Burke, and Ernzerhof (PBE) functionals which is based on the generalized gradient approximation (GGA).⁶⁰ We included onsite Coulomb interactions with Hubbard- U terms⁶¹ (PBE+ U) for strongly correlated elements with d -orbitals, such as Ti and Mo.

The effective U parameters for Ti and Mo used were 4.0 eV⁶² and 5.0 eV⁶³, respectively. Spin-polarized calculations were carried out with a $5 \times 5 \times 2$ k -mesh. Grimme's D3 dispersion correction⁶⁴ was also used to treat van der Waals interactions. For the analysis of delithiated states of TSS-HS and TSS-HE, Monte Carlo simulations were performed to identify the preferred Li-ion sites at various Li-concentrations (that is, for lithiated to fully de-lithiated states: 100.0, 87.5, 75.0, 67.5, 50.0, 32.5, 25.0, 12.5, 0.0). Using the Ising model, we determined initial guess ground state magnetic configurations of TSS-HS and TSS-HE systems for the DFT calculations. Three of the 20,000 potential spin configurations were taken into consideration for DFT calculations. The lowest energy structure obtained using DFT was considered for final calculations and analysis. We found that TSS-HS prefers a ferromagnetic state, while TSS-HE prefers an antiferromagnetic state as the ground state magnetic ordering. For the plane-wave basis set, we employed a 520 eV kinetic energy cut-off. In geometry optimizations, the force per atom convergence was 0.01 eV/Å, whereas the convergence criterion for self-consistent field electronic structure computations were 1×10^{-5} eV.

To determine the strength of metal-anion bonds at various Li-concentrations (metal=Ti, Mo and Al; anion=S and Se), we performed partial crystal orbital Hamilton population (pCOHP) analysis using the LOBSTER package.⁶⁵⁻⁶⁸ Maximum bond distances between Ti-S/Se, Mo-S, and Al-Se were between 1-3 Å for the pCOHP calculations. This analysis provides clues regarding the 'high entropy' effect on structural deformation of the TSS under the effect of Li-extraction.

Furthermore, to obtain the voltage profile of Li-(de)intercalation of TSS-HS and TSS-HE, the following expression was used:⁶⁹⁻⁷¹

$$V = - \frac{[E(Li_{x+dx}TSS) - E(Li_xTSS)]}{dx} + E(Li_{bcc}) \quad (2)$$

Here, $E(Li_{x+dx}TSS)$ and $E(Li_xTSS)$ are the energies per formula unit of TSS-HS (or TSS-HE) at $x + dx$ and x Li-concentrations. $E(Li_{bcc})$ is the energy per formula unit of bulk Li metal.

We also explored the relative performance of TSS-HS and TSS-HE anode materials forming an interface with a basic, common electrolyte composed of EC:PC (1:1) organic solvent molecules with 1M LiPF₆ salt.^{72, 73} To analyze the formation of a solid-electrolyte interface (SEI) between the anode (TSS-HS/TSS-HE) and the electrolyte we used ab-initio molecular dynamics simulations (AIMD) as implemented in VASP^{57, 58} at finite temperature (T=300K). These simulations demand significant computational resources, and therefore we used a reduced $3 \times 3 \times 2$ k-mesh.⁷⁴ The canonical ensemble (NVT) with the Nose-Hoover thermostat as a heat bath was employed. A time step of 1.0 fs and a total of 4 ps simulation time was considered. Our motivation for designing 'high entropy' anode-electrolyte interface is to achieve faster Li⁺ ions diffusion across the interface for improved ionic mobility and better electrochemical performance of the battery. The diffusion coefficient of Li-ions is determined by using mean square displacement (MSD) as follows:^{75, 76}

$$MSD(t) = \langle [r(t) - r(0)]^2 \rangle \quad (3)$$

Employing the Einstein formula, we obtain the diffusion coefficient as follows:

$$D = \frac{1}{6} \frac{d \text{MSD}(t)}{dt} \quad (4)$$

These equations are only approximate single particle diffusion equations rather than cooperative multi-ion diffusion equations. We used Packmol software⁷⁷ to create the optimized anode-electrolyte interface. The electrode-electrolyte interface modelled for AIMD simulations is shown in Fig 1(c).

Results and Discussion

1. Bulk Properties

1.1 Structural Stability

The pristine and high-entropy bulk HS composed of alternating layers of TiS_2 and TiSe_2 are shown in Fig 1 (a, b). The initial lattice parameters were chosen from the parent layered material TiSe_2 ⁷⁸ which were then allowed to fully relax to obtain the structural parameters of the complete HS. The lattice parameters obtained from TSS-HS and TSS-HE systems are listed Table 1.

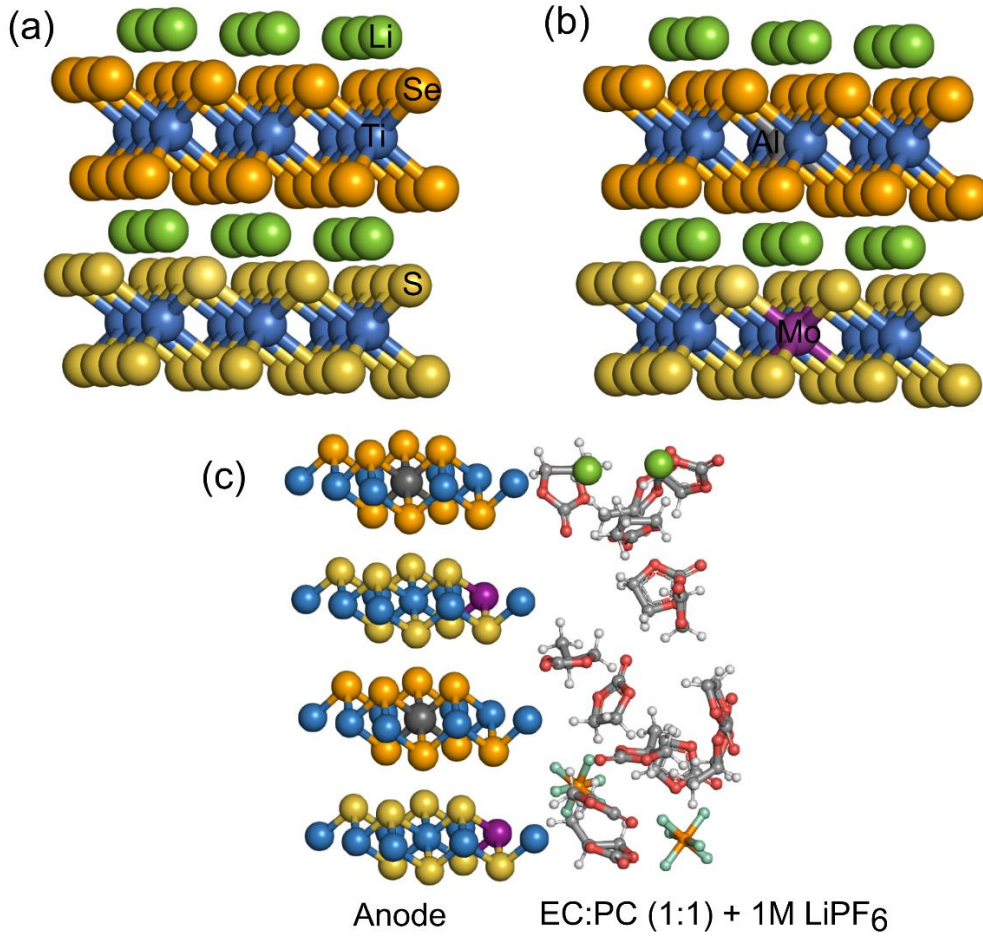


Figure 1: Optimized crystal structures of (a) TSS-HS and (b) TSS-HE. (c) Electrode-electrolyte interface obtained from Packmol.⁷⁷

These parameters are obtained without intercalating any Li-ion within the layers of HS. The overall lattice mismatch obtained in TSS-HS and TSS-HE *w.r.t* parent material TiSe_2 lattice parameter ' a ' is 0.28% and 2.52% which is quite low and considered within the limits of small mismatch.⁷⁹

Table 1: DFT calculated lattice parameters using PBE-U-D3 for TSS-HS, TSS-HE, and the reference heterostructure material TiSe_2 .

Structure	' a ' (Å)	' c ' (Å)	volume (Å ³)
TSS-HS	3.58	5.84	53.68
TSS-HE	3.66	5.87	56.47
TiSe_2	3.57 ⁷⁸ , 3.533 ⁸⁰	5.995 ⁸⁰	69.54

To identify low energy sites for Li-ions we calculated the ground state energy of four different available intercalation sites as shown in Fig 2 (inset). The lowest energy was obtained at site-1 (i.e., atop the Ti-site, E_1) and the energies for all other sites are provided in Fig 2 using the energy of site-1 as the reference. All other sites have relative energies, $\Delta E \gtrsim 1.0$ eV. For further calculations site-1 was considered for Li-intercalation, and 100% Li-coverage was used for fully lithiated layered anode materials.

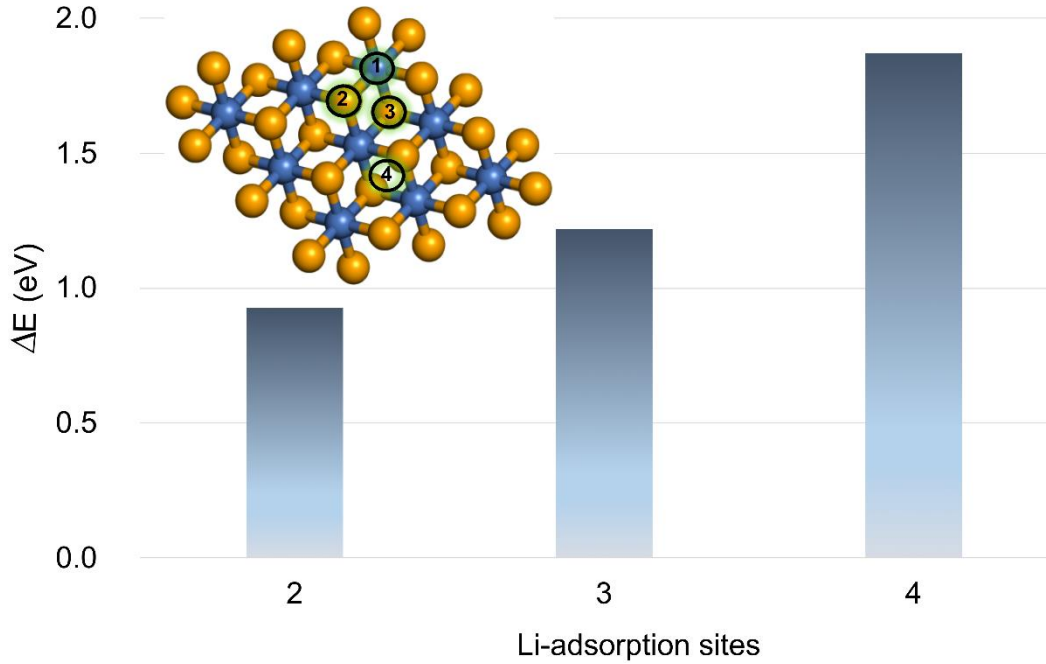


Figure 2: The difference in ground state energies of all considered sites relative to site-1. Li-intercalation sites labeled 1, 2, 3, and 4 viewed along the ' c '-axis(inset).

Furthermore, in order analyze the effect of 'high-entropy' on the structural changes in the layered anode TSS-HS, the relative change in structural parameters ' a ', ' c ' and *volume* are shown in Fig 3. In Fig 3a, ' a ' exhibits a pronounced decreasing trend with lithiation (that is, charging) up to 50% Li-concentration in TSS-HE, while subsequent lithiation ($\text{Li} > 50\%$) results in a smaller reduction in ' a '. In TSS-HS, ' a ' shows a continuous, albeit somewhat erratic, shrinkage as a function of Li-concentration, which overall is greater than for the high entropy material. We ascribe this shrinkage to reduced intralayer repulsion between metal ions as they are reduced. The ' c '

parameter changes only slightly as a function of lithiation up to 75%, while there is a drastic reduction upon complete lithiation for both TSS-HS and TSS-HE, which is also mirrored in the volume behavior. We ascribe this shrinkage to reduced interlayer repulsion between Se and S because of Li-ion intercalation between the TiS_2 and TiSe_2 layers. We further note that the overall change in the ' c ' parameter and volume is less for the high entropy material.

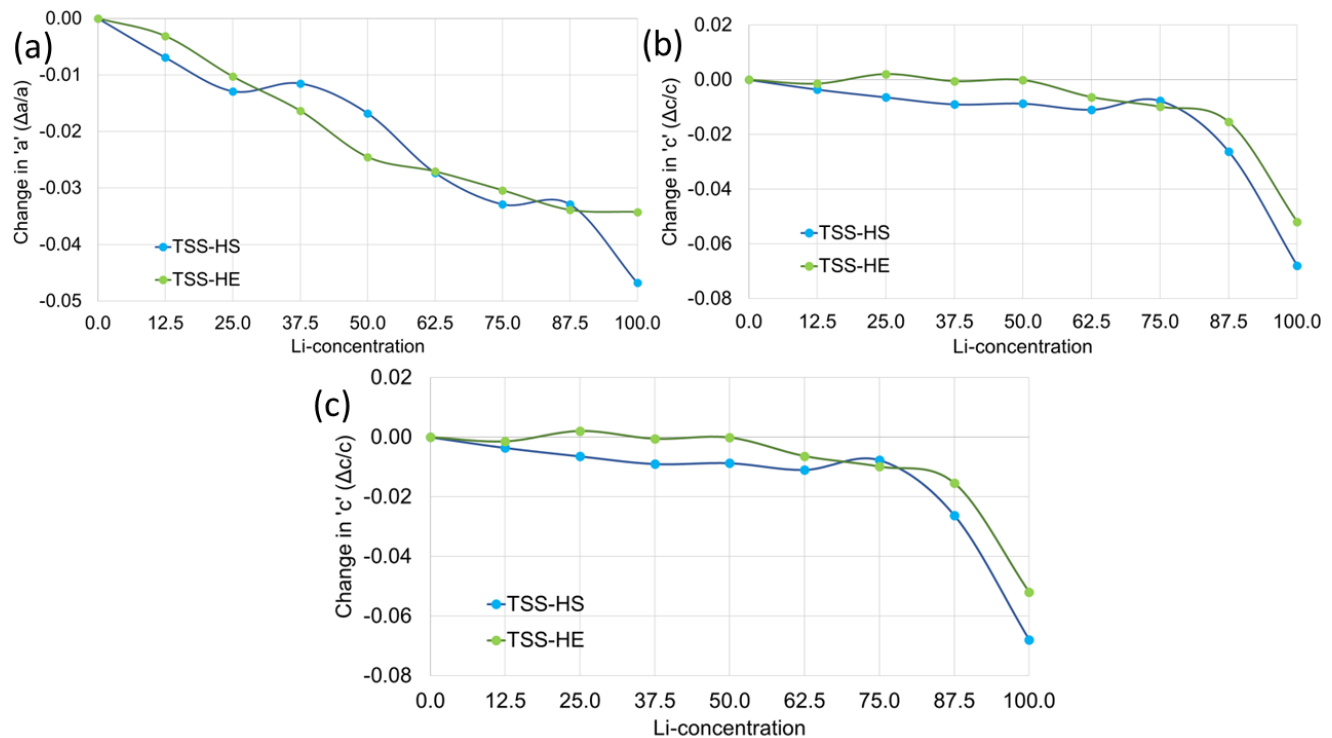


Figure 3: Relative change in (a) ' a ' lattice parameter, (b) ' c ' parameter and (c) *volume* of TSS-HS and TSS-HE as a function of Li-concentration.

Similar trends were observed in *volume* change as well (Fig 3c). Suppressed structural deformation attributed to 'entropy-stabilization' in during dis-charging also been reported by several groups.^{50, 81} Low lattice deformation may offer enhanced specific capacity as well as prolonged electrochemical cycling.

2. Electronic Structure

We performed electronic structure calculations to analyze the effect of 'high-entropy' on the electronic structure and electron-mobility in TSS anode materials. Partial density of states (PDOS) obtained for HS and HE at different Li-concentrations are provided in Fig 4, S1 and Fig 5, S2, respectively. Initially at Li-0%, TSS-HS have Ti^{4+} ions which consists of *zero* unpaired d -electrons, thus contributing no magnetic moment. This can also be observed in the Li-0% PDOS, where the spin-up and spin-down channels have identically occupied energy levels. The majority of the Ti^{4+} - d states are found in the conduction band region and no-energy gap is present. Upon lithiation of TSS-HS, the Ti-ions commence redox-activity, that is Ti^{4+} ions are reduced to Ti^{3+} ions. Ultimately all Ti^{4+} -ions are reduced to Ti^{3+} ions at the Li-100% level. We see that the Ti^{4+} - d states shifted down in energy upon Li-insertion as these ions are being reduced. The Ti^{3+} ion have an unpaired electron, and hence a *non-zero* magnetic moment is obtained for the Ti^{3+} - d states, which are located across the energy

spectrum. As expected, Se-*p* states are observed near the Fermi level, somewhat higher than the S-*p* states. No significant change in the chalcogen ions electronic states are observed with lithiation in TSS-HS, suggestion no detectable anion redox. At the 100% Li-level, a band gap of ~ 0.32 eV is observed, which may impede electron mobility in deep-discharged states of the anode.

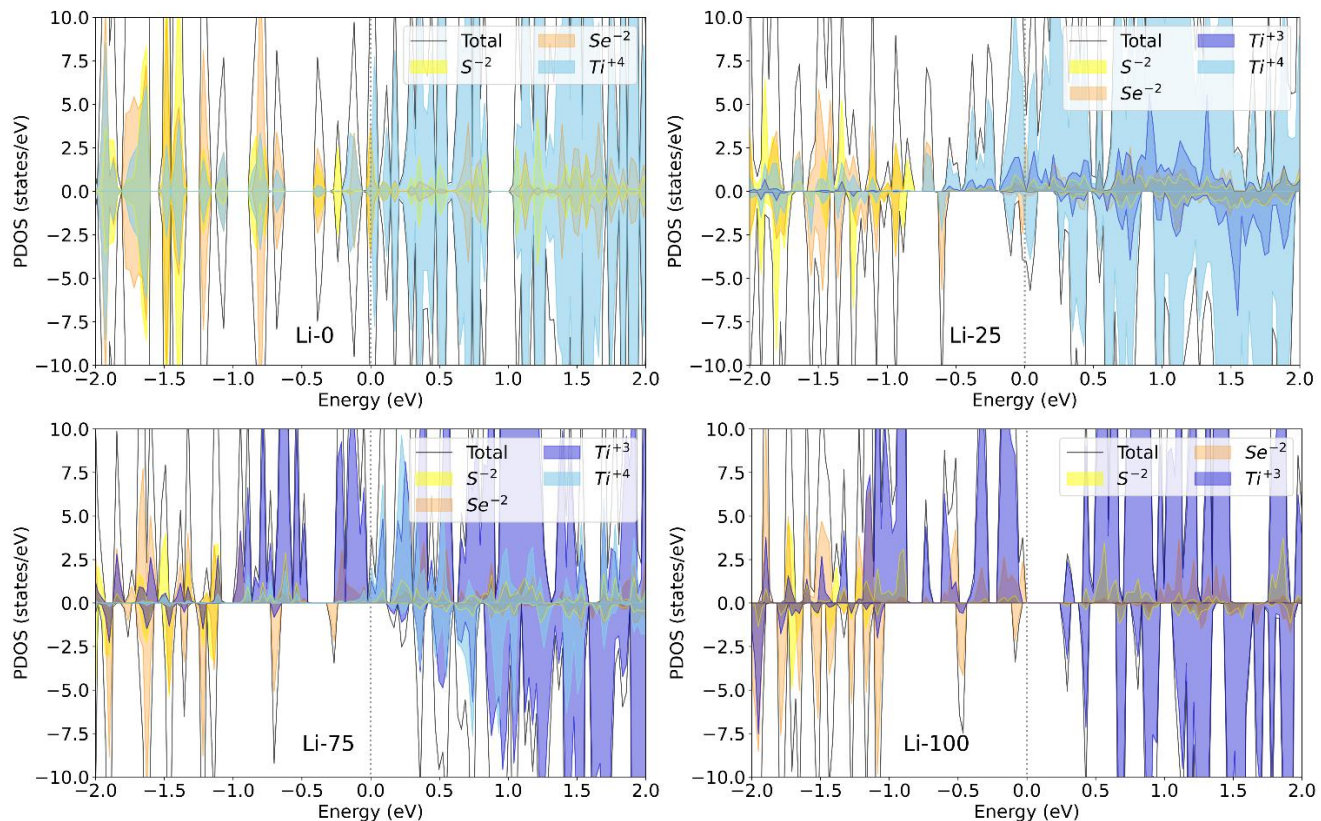


Figure 4: Partial density of states of TSS-HS at different Li-concentrations (Li-0 to 100%). The dotted line indicates that the Fermi level was set at 0.0 eV.

The PDOS of the high-entropy anode TSS-HE (Fig 5, Fig S2) shows similar trends for the $\text{Ti}^{4+} \rightarrow \text{Ti}^{3+}$ reduction with lithiation. The dopants Mo^{6+} and Al^{3+} were not found to change oxidation states during lithiation, suggesting no direct participation in redox, similar to what has been observed for cathode doping and high entropy materials.^{50, 63, 82, 83} However, Mo^{6+} has high-spin states with *non-zero* magnetic moment, whereas the electronic states of Al^{3+} are not spin polarized.

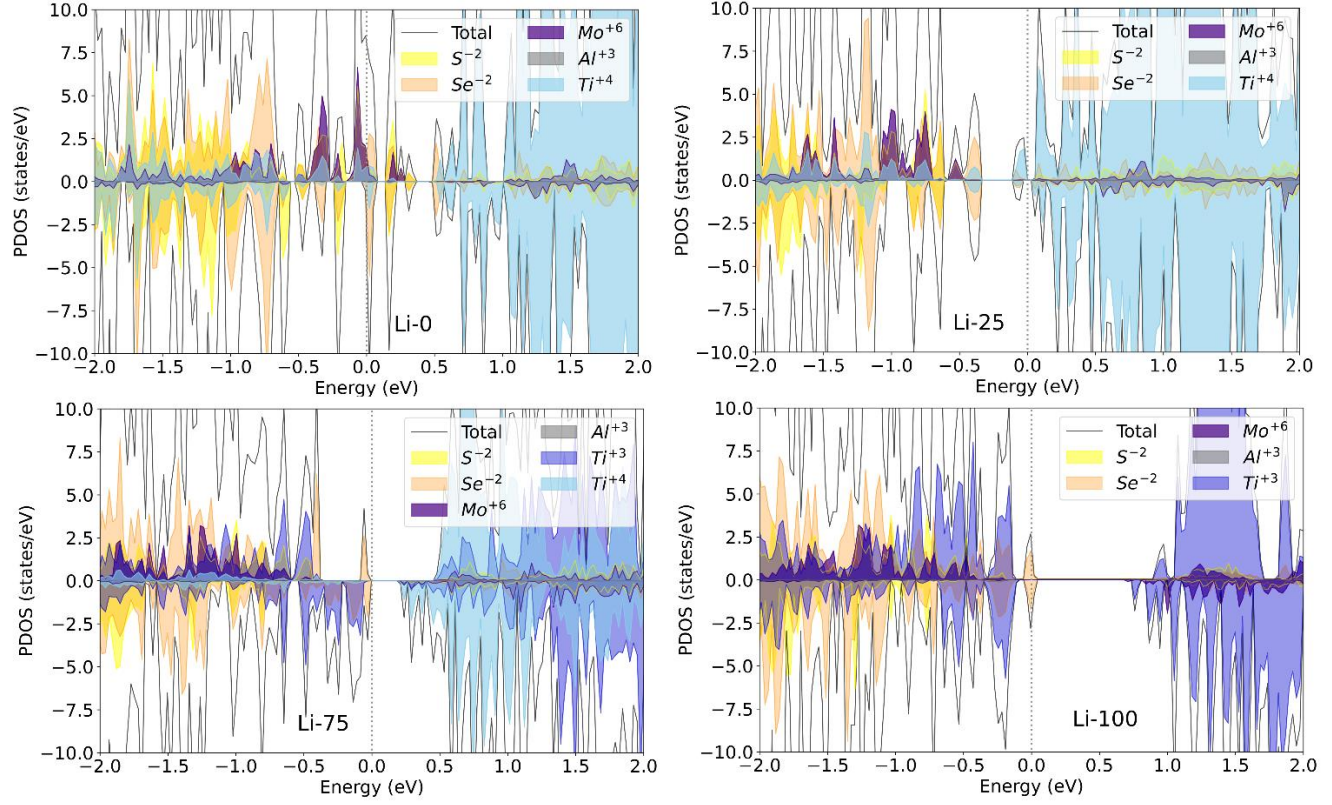


Figure 5: Partial density of states of TSS-HE at different Li-concentrations (Li-0 to 100%). The dotted line indicates that the Fermi level was set at 0.0 eV.

The high-valent dopant (i.e., Mo^{6+}) in TSS-HE adds conductive states into the Fermi level region, resulting in a zero-band gap at the 100% Li-level. This may offer improved electron mobility in deep discharged states resulting in better conductivity.

3. Redox Activity and Bond Strength

In the PDOS analysis, we found that Ti-ions are redox-active, while the chalcogen- and dopant ions do not change their oxidation states during lithiation. For a closer look at the redox activity of the Ti-ions with Li-concentration, we performed redox population analysis for TSS-HS and TSS-HE anode materials. In both TSS-HS and TSS-HE, all Ti-ions are found in a Ti^{4+} oxidation state (Fig 6). In TSS-HS Ti^{3+} begin to appear at Li-25%, while in TSS-HE Ti^{3+} emerge at Li-37.5%. In TSS-HS, all Ti^{4+} are consumed by Li-25%, while for TSS-HE this only occurs at Li-100%. Hence, the onset of Ti-reduction is shifted slightly to greater lithiation levels in the high entropy material. We note that the presence of Ti^{4+} ions is important to maintain a consistent and strong bonding environment with surrounding Se and S ions. Additionally, it has been reported that Mo^{6+} and Al^{3+} ions offer strong bonding with surrounding anions which can lead to improved material stability.^{50, 63, 83, 84}

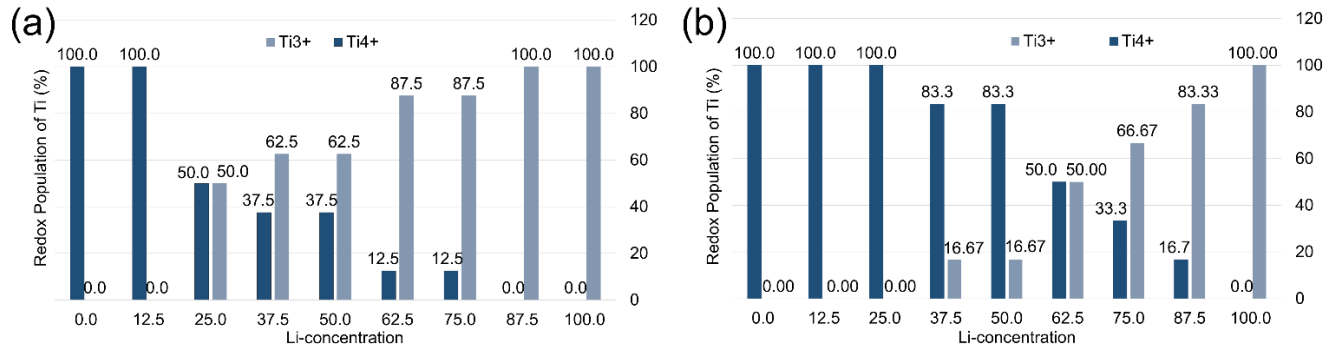


Figure 6: Redox population of Ti-ions as a function of Li-concentration in (a) TSS-HS and (b) TSS-HE.

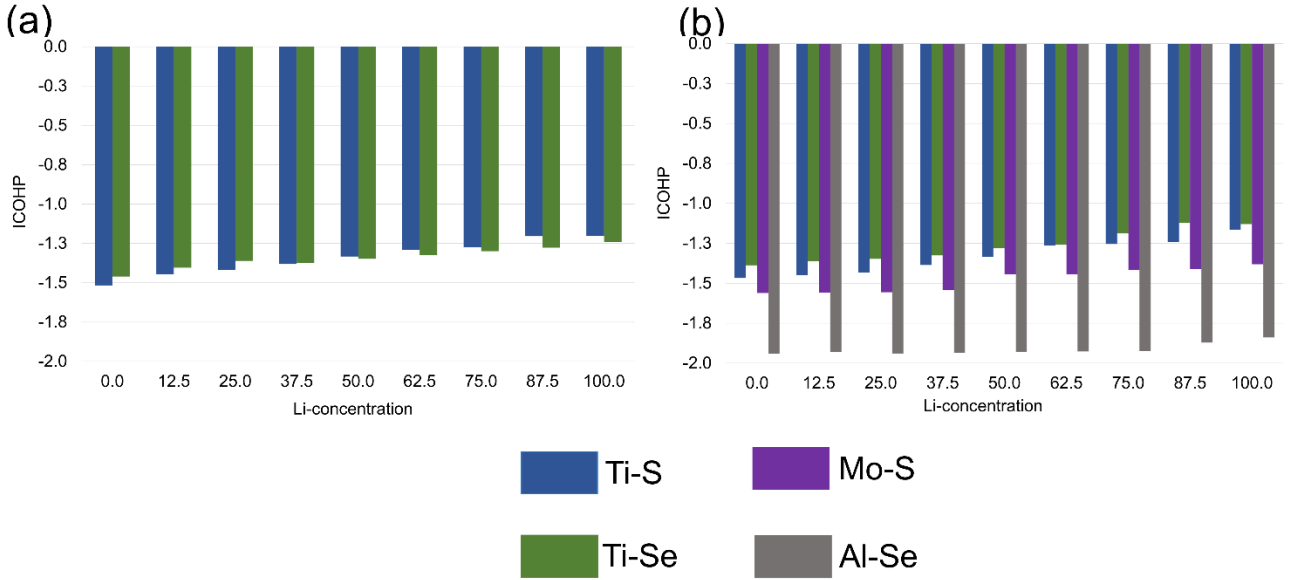


Figure 7: Metal-Chalcogen ion bonding in (a) TSS-HS and (b) TSS-HE, showing the change in bond strength at different Li-concentration levels. Values of ICOHP (y-axis) are obtained as the integrated COHP at the Fermi Level.

To quantify the strength of chalcogen-metal bonds in the TSS materials, we performed ICOHP analyses, where more negative ICOHP values indicate stronger bonds. The ICOHP as a function of Li-concentration can be seen in Fig 7 (a) and (b) for TSS-HS and TSS-HE anode materials, respectively. From Fig 7 we observe that Ti-S and Ti-Se bonding is weakened with lithium insertion for both TSS-HS and TSS-HE, which may be attributed to $\text{Ti}^{4+} \rightarrow \text{Ti}^{3+}$ reduction. However, in Fig 7(b) we see that the dopants Mo^{6+} and Al^{3+} form much stronger bonds with surrounding chalcogen ions. This could be a factor in preventing structural deformations with lithiation in TSS-HE.

4. Theoretical Specific Capacity and Voltage Profile

In designing high-performance LIBs, theoretical specific capacity (C) is a crucial factor, which depends on the concentration of intercalated active ions (i.e., Li^+ -ions). The theoretical capacity can be determined using the following expression:²⁴

$$C = \frac{c_{\max} F}{M} \quad (5)$$

where c_{\max} indicates the maximum concentration of intercalated Li^+ ions per formula unit of the electrode. F is Faraday's constant ($26,801 \text{ mA}\cdot\text{h}\cdot\text{mol}^{-1}$) and M is the molecular mass of the anode material. Maximum capacity of intercalation is

associated with fully lithiated anode materials (TSS-HS and TSS-HE). The calculated theoretical specific capacity using *equation (5)* for TSS-HS and TSS-HE are $337.34 \text{ mA}\cdot\text{h}\cdot\text{g}^{-1}$ and $370.71 \text{ mA}\cdot\text{h}\cdot\text{g}^{-1}$ respectively which is better than for previously reported TiS_2 and TiSe_2 based^{85, 86} and other layered heterostructures.⁸⁷⁻⁸⁹

A comparative analysis of specific capacity of our work and available layered anode materials is also provided in Fig 8 which indicates an improved capacity of TSS-HS and TSS-HE both anode materials.

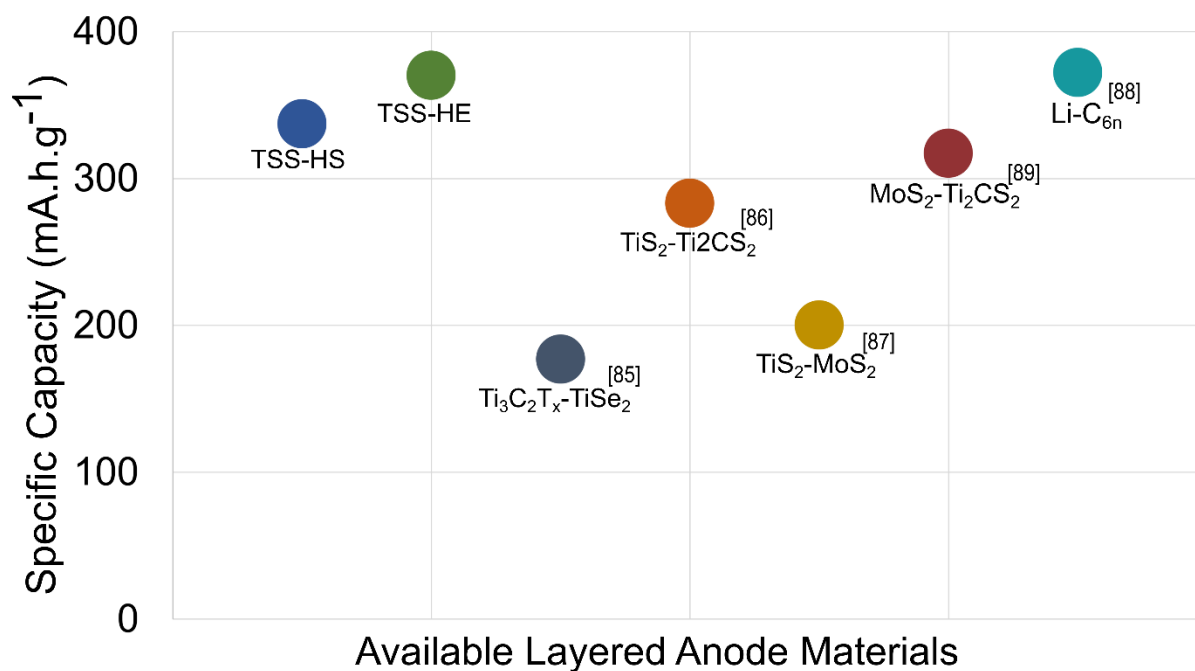


Figure 8: A comparative analysis of specific capacity obtained for TSS-HS (Blue) and TSS-HE (orange) with other available layered anode materials.

A higher capacity may arise because of suppressed structural deformation of TSS-HE attributed to 'entropy stabilization' effect with low internal strain.

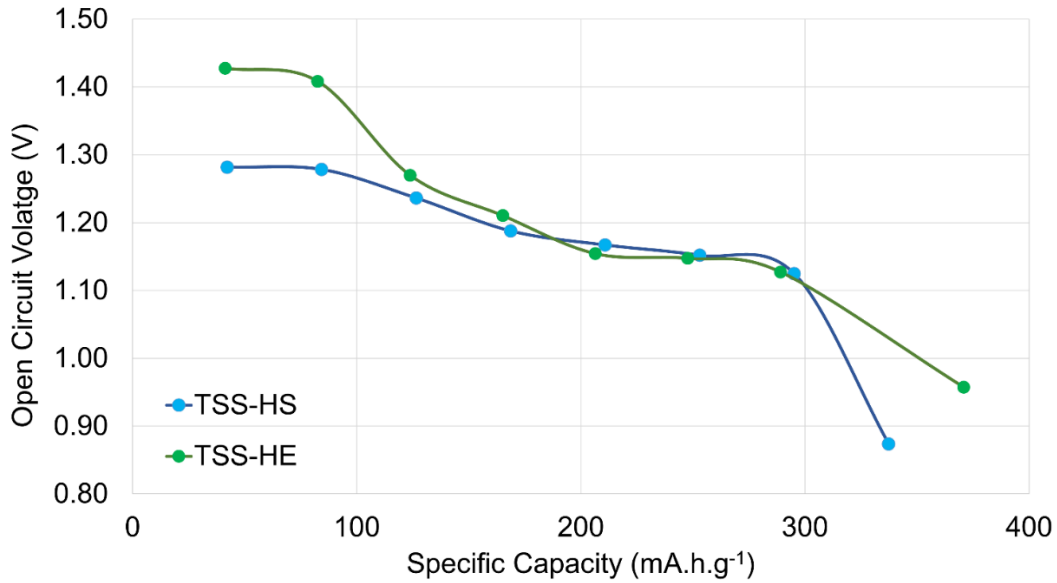


Figure 9: DFT calculated open circuit voltage versus theoretical specific capacity for TSS-HS and TSS-HE.

The operational voltage and corresponding specific capacity for both anode materials were obtained from *equations (2) and (5)* (Fig 9). A higher capacity and a wider operational voltage window (~ 0.47 V) are achieved in TSS-HE as compared to TSS-HS (~ 0.40 V). We ascribe this to better structural stability accompanied with suppressed volumetric strain in TSS-HE anode.

5. Interface properties

Prior to studying the Li diffusion behavior at the EEI, the structural evolution and Li diffusion in a model electrolyte (EC, PC, and PF_6^-) was analyzed by computing the integrated radial distribution function (IRDF) (Fig 10(a,b)). We considered a relatively short simulations⁹⁰⁻⁹² to establish basic qualitative trends relating to ion-transport in TSS-HS and TSS-HE at the EEI. Our IRDF analyses show that Li^+ ion coordination with surrounding molecules in the electrolyte decreases in the TSS-HE-electrolyte complex (Fig 10(b)) compared to the TSS-HS-electrolyte (Fig 10(a)), with values of 1.90 to 1.33 (Li-O (EC)) and 1.05 to 0.65 (Li-O (PC)), respectively, within an interaction distance of 3 Å. Reduced coordination of Li ions can offer better mobility near the EEI and thus results in better diffusion. Additionally, we can also predict from IRDF results that the primary solvation shell at the EEI will mainly be composed of EC and PC molecules.⁹³

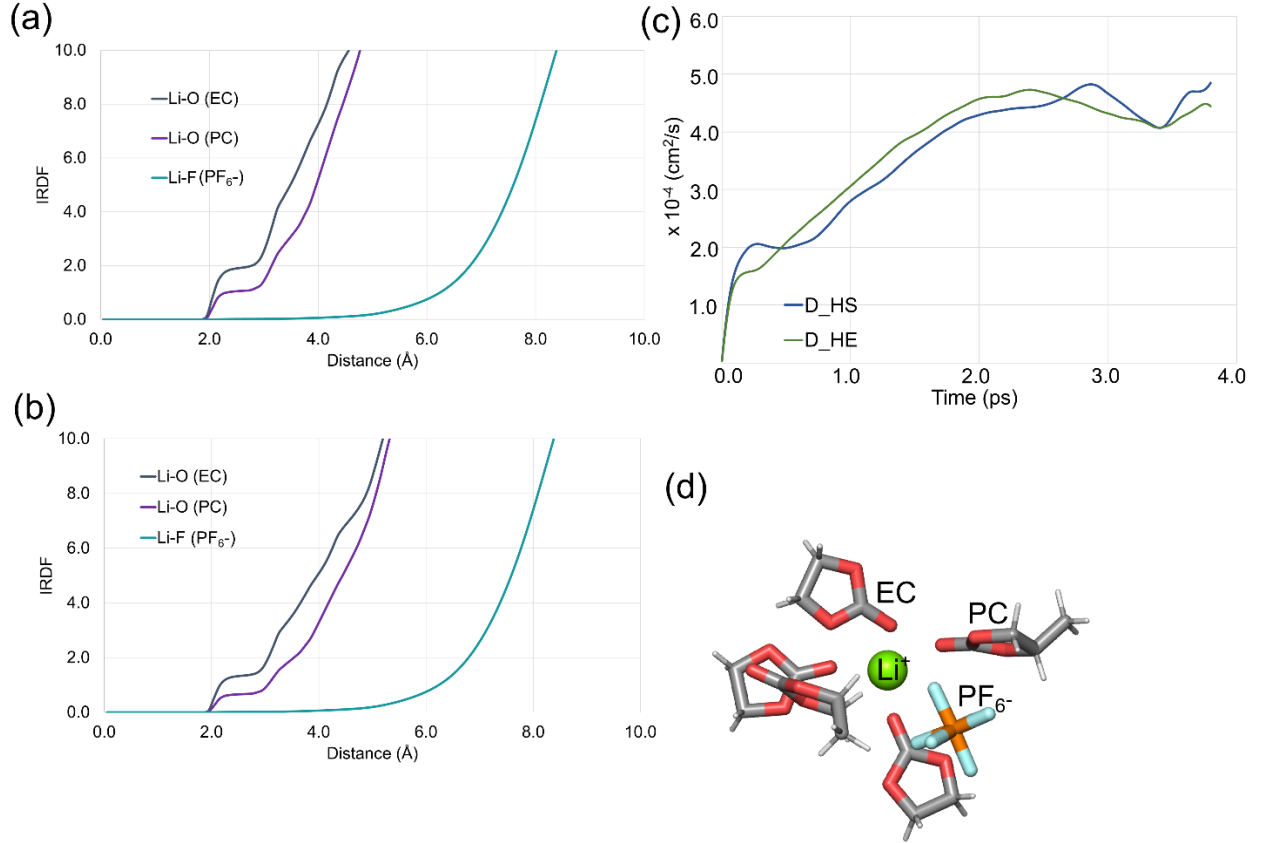


Figure 10: Integrated radial distribution function $n(r)$ obtained with AIMD simulations of Li-ion and its surrounding organic solvents (EC and PC) and salt (PF₆) for anode materials (a) TSS-HS and (b) TSS-HE. (c) Diffusion coefficient of Li-ions at the EEI interface showing slightly faster diffusion at the TSS-HE:Electrolyte interface (D_HE), compared to the TSS-HS:Electrolyte interface (D_HS), (d) Snapshot of a Li⁺ ion and its surrounding electrolyte environment within a radius of 4 Å.

The diffusion coefficients of Li ions obtained from a linear fit of the MSD using *equation (4)* are shown in Fig 10(c). We observe that at the EEI with TSS-HE, there is slightly faster Li diffusion compared to EEI with TSS-HS. The average diffusion coefficient and ionic mobility obtained are listed in Table 2.

Table 2: Computed average diffusion coefficient and ionic mobility at 300K.

EEI	Average Diffusion Coefficient ($\times 10^{-4} \text{ cm}^2/\text{s}$)	Average Ionic Mobility ($\times 10^{-2} \text{ cm}^2/\text{s/V}$)
TSS-HS: Electrolyte	4.67 ± 0.067	1.81 ± 0.028
TSS-HE: Electrolyte	5.35 ± 0.095	2.10 ± 0.079

Conclusions

To investigate the effect of high entropy on the layered bulk heterostructure anode material TSS, we performed DFT calculations of several properties relevant to electrochemistry. We performed DFT calculations of properties as a function of Li-concentration and propose that TSS-HE anode materials might experience less structural deformations, while possessing better electron mobility, bond strengths, and higher theoretical specific capacity than the low-entropy analogue. Specifically, our calculations suggest that the presence of elements like Mo⁶⁺ and Al³⁺ provide lower

internal strain (less volumetric change), stronger bonds, as well as better electron mobility. We, performed AIMD simulations where the IRDF, average diffusion coefficient, and average ionic mobility suggest slightly improved ion-transport for the TSS-HE anode near the EEL. In summary, our work provides atomistic level insights into possible high entropy TSS anode materials for Li-ion batteries, and presents ideas for future experimental work.

References:

- .1 Kang, B.; Ceder, G., Battery materials for ultrafast charging and discharging. *Nature* **2009**, *458* (7235), 190-193.
- .2 Tarascon, J. M.; Armand, M., Issues and challenges facing rechargeable lithium batteries. *Nature* **2001**, *414* (6861), 359-367.
- .3 Zhang, Q.; Liu, Y.; Lu, H.; Tang, D.; Ouyang, C.; Zhang, L., Ce³⁺-doped Li₄Ti₅O₁₂ with CeO₂ surface modification by a sol-gel method for high-performance lithium-ion batteries. *Electrochimica Acta* **2016**, *189*, 147-157.
- .4 Zhou, G.; Li, F.; Cheng, H.-M., Progress in flexible lithium batteries and future prospects. *Energy & Environmental Science* **2014**, *7* (4), 1307-1338.
- .5 Britnell, L.; Gorbachev, R. V.; Jalil, R.; Belle, B. D.; Schedin, F.; Mishchenko, A.; Georgiou, T.; Katsnelson, M. I.; Eaves, L.; Morozov, S. V.; Peres, N. M. R.; Leist, J.; Geim, A. K.; Novoselov, K. S.; Ponomarenko, L. A., Field-Effect Tunneling Transistor Based on Vertical Graphene Heterostructures. *Science* **2012**, *335* (6071), 947-950.
- .6 Raccichini, R.; Varzi, A.; Passerini, S.; Scrosati, B., The role of graphene for electrochemical energy storage. *Nature Materials* **2015**, *14* (3), 271-279.
- .7 Santos, J. E.; Peres, N. M. R.; Lopes dos Santos, J. M. B.; Castro Neto, A. H., Electronic doping of graphene by deposited transition metal atoms. *Physical Review B* **2011**, *84* (8), 085430.
- .8 Nistor, R. A.; Kuroda, M. A.; Maarouf, A. A.; Martyna, G. J., Doping of adsorbed graphene from defects and impurities in SiO₂ substrates. *Physical Review B* **2012**, *86* (4), 041409.
- .9 Guinea, F.; Katsnelson, M. I.; Geim, A. K., Energy gaps and a zero-field quantum Hall effect in graphene by strain engineering. *Nature Physics* **2010**, *6* (1), 30-33.
- .10 Choi, S.-M.; Jhi, S.-H.; Son, Y.-W., Effects of strain on electronic properties of graphene. *Physical Review B* **2010**, *81* (8), 081407.
- .11 Lahiri, J.; Lin, Y.; Bozkurt, P.; Oleynik, I. I.; Batzill, M., An extended defect in graphene as a metallic wire. *Nature Nanotechnology* **2010**, *5* (5), 326-329.
- .12 Paton, K. R.; Varrla, E.; Backes, C.; Smith, R. J.; Khan, U.; O'Neill, A.; Boland, C.; Lotya, M.; Istrate, O. M.; King, P.; Higgins, T.; Barwich, S.; May, P.; Puczkarski, P.; Ahmed, I.; Moebius, M.; Pettersson, H.; Long, E.; Coelho, J.; O'Brien, S. E.; McGuire, E. K.; Sanchez, B. M.; Duesberg, G. S.; McEvoy, N.; Pennycook, T. J.; Downing, C.; Crossley, A.; Nicolosi, V.; Coleman, J. N., Scalable production of large quantities of defect-free few-layer graphene by shear exfoliation in liquids. *Nature Materials* **2014**, *13* (6), 624-630.
- .13 Georgiou, T.; Jalil, R.; Belle, B. D.; Britnell, L.; Gorbachev, R. V.; Morozov, S. V.; Kim, Y.-J.; Gholinia, A.; Haigh, S. J.; Makarovskiy, O.; Eaves, L.; Ponomarenko, L. A.; Geim, A. K.; Novoselov, K. S.; Mishchenko, A., Vertical field-effect transistor based on graphene-WS₂ heterostructures for flexible and transparent electronics. *Nature Nanotechnology* **2013**, *8* (2), 100-103.
- .14 Hunt, B.; Sanchez-Yamagishi, J. D.; Young, A. F.; Yankowitz, M.; LeRoy, B. J.; Watanabe, K.; Taniguchi, T.; Moon, P.; Koshino, M.; Jarillo-Herrero, P.; Ashoori, R. C., Massive Dirac Fermions and Hofstadter Butterfly in a van der Waals Heterostructure. *Science* **2013**, *340* (6139), 1427-1430.

- .15 Hong, X.; Kim, J.; Shi, S.-F.; Zhang, Y.; Jin, C.; Sun, Y.; Tongay, S.; Wu, J.; Zhang, Y.; Wang, F., Ultrafast charge transfer in atomically thin MoS₂/WS₂ heterostructures. *Nature Nanotechnology* **2014**, *9* (9), 682-686.
- .16 Allain, A.; Kang, J.; Banerjee, K.; Kis, A., Electrical contacts to two-dimensional semiconductors. *Nature Materials* **2015**, *14* (12), 1195-1205.
- .17 Roy, T.; Tosun, M.; Kang, J. S.; Sachid, A. B.; Desai, S. B.; Hettick, M.; Hu, C. C.; Javey, A., Field-Effect Transistors Built from All Two-Dimensional Material Components. *ACS Nano* **2014**, *8*, 6259-6264, (6)
- .18 Koppens, F. H. L.; Mueller, T.; Avouris, P.; Ferrari, A. C.; Vitiello, M. S.; Polini, M., Photodetectors based on graphene, other two-dimensional materials and hybrid systems. *Nature Nanotechnology* **2014**, *9* (10), 780-793.
- .19 Mehew, J. D.; Unal, S.; Torres Alonso, E.; Jones, G. F.; Fadhil Ramadhan, S.; Craciun, M. F.; Russo, S., Fast and Highly Sensitive Ionic-Polymer-Gated WS₂-Graphene Photodetectors. *Advanced Materials* **2017**, *29* (23), 1700222.
- .20 Kumar, P.; Lynch, J.; Song, B.; Ling, H.; Barrera, F.; Kisslinger, K.; Zhang, H.; Anantharaman, S. B.; Digani, J.; Zhu, H.; Choudhury, T. H.; McAleese, C.; Wang, X.; Conran, B. R.; Whear, O.; Motala, M. J.; Snure, M.; Muratore, C.; Redwing, J. M.; Glavin, N. R.; Stach, E. A.; Davoyan, A. R.; Jariwala, D., Light-matter coupling in large-area van der Waals superlattices. *Nature Nanotechnology* **2022**, *17* (2), 182-189.
- .21 Samad, A.; Noor-A-Alam, M.; Shin, Y.-H., First principles study of a SnS₂/graphene heterostructure :a promising anode material for rechargeable Na ion batteries. *Journal of Materials Chemistry A* **2016**, *4* (37), 14316-14323.
- .22 Guo, G.-C.; Wang, D.; Wei, X.-L.; Zhang, Q.; Liu, H.; Lau, W.-M.; Liu, L.-M., First-Principles Study of Phosphorene and Graphene Heterostructure as Anode Materials for Rechargeable Li Batteries. *The Journal of Physical Chemistry Letters* **2015**, *6* (24), 5002-5008.
- .23 Shao, X.; Wang, K.; Pang, R.; Shi, X., Lithium Intercalation in Graphene/MoS₂ Composites: First-Principles Insights. *The Journal of Physical Chemistry C* **2015**, *119* (46), 25860-25867.
- .24 Barik, G.; Pal, S., 2D MoS₂-MoSe₂ and MoS₂-NbS₂ lateral heterostructures as anode materials for LIBs/SIBs. *Applied Surface Science* **2022**, *596*, 153529.
- .25 Vishwanathan, S.; Chithaiah, P.; Matte, H. S. S. R.; Rao, C. N. R., 3R-NbS₂ as a highly stable anode for sodium-ion batteries. *Chemical Communications* **2024**, *60* (10), 1309-1312.
- .26 Xu, B.; Ma, X.; Tian, J.; Zhao, F.; Liu, Y.; Wang, B.; Yang, H.; Xia, Y., Layer-structured NbSe₂ anode material for sodium-ion and potassium-ion batteries. *Ionics* **2019**, *25* (9), 4171-4177.
- .27 Du, G.; Guo, Z.; Wang, S.; Zeng, R.; Chen, Z.; Liu, H., Superior stability and high capacity of restacked molybdenum disulfide as anode material for lithium ion batteries. *Chemical Communications* **2010**, *46* (7), 1106-1108.
- .28 Li, W.; Yang, Y.; Zhang, G.; Zhang, Y.-W., Ultrafast and Directional Diffusion of Lithium in Phosphorene for High-Performance Lithium-Ion Battery. *Nano Letters* **2015**, *15* (3), 1691-1697.
- .29 Tritsarlis, G. A.; Kaxiras, E.; Meng, S.; Wang, E., Adsorption and Diffusion of Lithium on Layered Silicon for Li-Ion Storage. *Nano Letters* **2013**, *13* (5), 2258-2263.
- .30 Li, Y.; Wu, D.; Zhou, Z.; Cabrera, C. R.; Chen, Z., Enhanced Li Adsorption and Diffusion on MoS₂ Zigzag Nanoribbons by Edge Effects: A Computational Study. *The Journal of Physical Chemistry Letters* **2012**, *3* (16), 2221-2227.
- .31 Chhowalla, M.; Shin, H. S.; Eda, G.; Li, L.-J.; Loh, K. P.; Zhang, H., The chemistry of two-dimensional layered transition metal dichalcogenide nanosheets. *Nature Chemistry* **2013**, *5* (4), 263-275.

- .32 Price, C. J.; Baker, E. A. D.; Hepplestone, S. P., Properties of Layered TMDC Superlattices for Electrodes in Li-Ion and Mg-Ion Batteries. *The Journal of Physical Chemistry C* **2024**, 128 (5), 1867-1876.
- .33 Wang, D.; Liu, L.-M.; Zhao, S.-J.; Hu, Z.-Y.; Liu, H., Potential Application of Metal Dichalcogenides Double-Layered Heterostructures as Anode Materials for Li-Ion Batteries. *The Journal of Physical Chemistry C* **2016**, 120 (9), 4779-4788.
- .34 Yun, Y.; Shao, J.; Shang, X.; Wang, W.; Huang, W.; Qu, Q.; Zheng, H., Simultaneously formed and embedding-type ternary MoSe₂/MoO₂/nitrogen-doped carbon for fast and stable Na-ion storage. *Nanoscale Advances*.1878-1885 ,(5) 2 ,2020
- .35 Molina-Mendoza, A. J.; Giovanelli, E.; Paz, W. S.; Niño, M. A.; Island, J. O.; Evangelii, C.; Aballe, L.; Foerster, M.; van der Zant, H. S. J.; Rubio-Bollinger, G.; Agraït, N.; Palacios, J. J.; Pérez, E. M.; Castellanos-Gomez, A., Franckeite as a naturally occurring van der Waals heterostructure. *Nature Communications* **2017**, 8 (1), 14409.
- .36 Yang, Y.; Fang, S.; Fatemi, V.; Ruhman, J.; Navarro-Moratalla, E.; Watanabe, K.; Taniguchi, T.; Kaxiras, E.; Jarillo-Herrero, P., Enhanced superconductivity upon weakening of charge density wave transport in 2H-TaS₂ in the two-dimensional limit. *Physical Review B* **2018**, 98 (3), 035203.
- .37 Nagata, S.; Aochi, T.; Abe, T.; Ebisu, S.; Hagino, T.; Seki, Y.; Tsutsumi, K., Superconductivity in the layered compound 2H-TaS₂. *Journal of Physics and Chemistry of Solids* **1992**, 53 (10), 1259-1263.
- .38 Sipos, B.; Kusmartseva, A. F.; Akrap, A.; Berger, H.; Forró, L.; Tutiš, E., From Mott state to superconductivity in 1T-TaS₂. *Nature Materials* **2008**, 7 (12), 960-965.
- .39 Zheng, R.; Yu, H.; Zhang, X.; Ding, Y.; Xia, M.; Cao, K.; Shu, J.; Vlad, A.; Su, B.-L., A TiSe₂-Graphite Dual Ion Battery: Fast Na-Ion Insertion and Excellent Stability. *Angewandte Chemie International Edition* **2021**, 60 (34), 18430-18437.
- .40 Zhang, D.; Zhao, G.; Li, P.; Zhang, Y.; Qiu, W.; Shu, J.; Jiang, Y.; Dou, S. X.; Sun, W., Readily Exfoliated TiSe₂ Nanosheets for High-Performance Sodium Storage. *Chemistry – A European Journal* **2018**, 24 (5), 1193.1197-
- .41 Li, W.; Wang, K.; Cheng, S.; Jiang, K., An Ultrastable Presodiated Titanium Disulfide Anode for Aqueous “Rocking-Chair” Zinc Ion Battery. *Advanced Energy Materials* **2019**, 9 (27), 1900993.
- .42 Wen, L.; Wu, Y.; Wang, S.; Shi, J.; Zhang, Q.; Zhao, B.; Wang, Q.; Zhu, C.; Liu, Z.; Zheng, Y.; Su, J.; Gao, Y., A novel TiSe₂ (de)intercalation type anode for aqueous zinc-based energy storage. *Nano Energy* **2022**, 93, 106896.
- .43 Zhang, L.; Hou, X.; Edström, K.; Berg, E. J., Reactivity of TiS₂ Anode towards Electrolytes in Aqueous Lithium-Ion Batteries. *Batteries & Supercaps* **2022**, 5 (12), e202200336.
- .44 Dong, Z.; Wu, X.; Chen, M.; Chen, H.; Huang, K.-J.; Wang, L.; Xu, J., Self-supporting 1T-MoS₂@WS₂@CC composite materials for potential high-capacity sodium storage system. *Journal of Colloid and Interface Science* **2023**, 630, 426-435.
- .45 Liu, H.; Huang, Z.; Wu, G.; Wu, Y.; Yuan, G.; He, C.; Qi, X.; Zhong, J., A novel WS₂/NbSe₂ vdW heterostructure as an ultrafast charging and discharging anode material for lithium-ion batteries. *Journal of Materials Chemistry A* **2018**, 6 (35), 17040-17048.
- .46 Zheng, Y.; Kong, X.; He, L.; Shang, J.; Wang, D.; Lei, C.; Zhao, Y., Constructing bimetallic heterostructure as anodes for sodium storage with superior stability and high capacity. *Journal of Power Sources* **2023**, 580, 233371.
- .47 Wang, Q.; Sarkar, A.; Wang, D.; Velasco, L.; Azmi, R.; Bhattacharya, S. S.; Bergfeldt, T.; Düvel, A.; Heitjans, P.; Brezesinski, T.; Hahn, H.; Breitung, B., Multi-anionic and -cationic compounds: new high entropy materials for advanced Li-ion batteries. *Energy & Environmental Science* **2019**, 12 (8), 2433-2442.

- .48 Ma, Y.; Ma, Y.; Wang, Q.; Schweidler, S.; Botros, M.; Fu, T.; Hahn, H.; Brezesinski, T.; Breitung, B., High-entropy energy materials: challenges and new opportunities. *Energy & Environmental Science* **2021**, *14* (5), 2883-2905.
- .49 Sarkar, A.; Velasco, L.; Wang, D.; Wang, Q.; Talasila, G.; de Biasi, L.; Kübel, C.; Brezesinski, T.; Bhattacharya, S. S.; Hahn, H.; Breitung, B., High entropy oxides for reversible energy storage. *Nature Communications* **2018**, *9* (1), 3400.
- .50 Bano, A.; Noked, M.; Major, D. T., Theoretical Insights into High-Entropy Ni-Rich Layered Oxide Cathodes for Low-Strain Li-Ion Batteries. *Chemistry of Materials* **2023**, *35* (20), 8426-8439.
- .51 Lun, Z.; Ouyang, B.; Kwon, D.-H.; Ha, Y.; Foley, E. E.; Huang, T.-Y.; Cai, Z.; Kim, H.; Balasubramanian, M.; Sun, Y.; Huang, J.; Tian, Y.; Kim, H.; McCloskey, B. D.; Yang, W.; Clément, R. J.; Ji, H.; Ceder, G., Cation-disordered rocksalt-type high-entropy cathodes for Li-ion batteries. *Nature Materials* **2021**, *20* (2), 214-221.
- .52 Zheng, W.; Liang, G.; Liu, Q.; Li, J.; Yuwono, J. A.; Zhang, S.; Peterson, V. K.; Guo, Z., The promise of high-entropy materials for high-performance rechargeable Li-ion and Na-ion batteries. *Joule* **2023**, *7* (12), 2732-2748.
- .53 Dippo, O. F.; Vecchio, K. S., A universal configurational entropy metric for high-entropy materials. *Scripta Materialia* **2021**, *201*, 113974.
- .54 Zhao, X.; Ceder, G., Zero-strain cathode materials for Li-ion batteries. *Joule* **2022**, *6* (12), 2683-2685.
- .55 Martha, S. K.; Nanda, J.; Veith, G. M.; Dudney, N. J., Electrochemical and rate performance study of high-voltage lithium-rich composition: $\text{Li}_{1.2}\text{Mn}_{0.525}\text{Ni}_{0.175}\text{Co}_{0.1}\text{O}_2$. *Journal of Power Sources* **2012**, *199*, 220-226.
- .56 Zeng, Y.; Ouyang, B.; Liu, J.; Byeon, Y.-W.; Cai, Z.; Miara, L. J.; Wang, Y.; Ceder, G., High-entropy mechanism to boost ionic conductivity. *Science* **2013**, *339* (6626), 1320-1324.
- .57 Kresse, G.; Hafner, J., Ab initio molecular-dynamics simulation of the liquid-metal-amorphous-semiconductor transition in germanium. *Physical Review B* **1994**, *49* (20), 14251-14269.
- .58 Kresse, G.; Furthmüller, J., Efficiency of ab-initio total energy calculations for metals and semiconductors using a plane-wave basis set. *Computational Materials Science* **1996**, *6* (1), 15-50.
- .59 Blöchl, P. E., Projector augmented-wave method. *Physical Review B* **1994**, *50* (24), 17953-17979.
- .60 Perdew, J. P.; Burke, K.; Ernzerhof, M., Generalized Gradient Approximation Made Simple. *Physical Review Letters* **1996**, *77* (18), 3865-3868.
- .61 Dudarev, S. L.; Botton, G. A.; Savrasov, S. Y.; Humphreys, C. J.; Sutton, A. P., Electron-energy-loss spectra and the structural stability of nickel oxide: An LSDA+U study. *Physical Review B* **1998**, *57* (3), 1505-1509.
- .62 Zhang, Z.; Hong, B.; Yi, M.; Fan, X.; Zhang, Z.; Huang, X.; Lai, Y., In situ co-doping strategy for achieving long-term cycle stability of single-crystal Ni-rich cathodes at high voltage. *Chemical Engineering Journal* **2022**, *445*, 136825.
- .63 Susai, F. A.; Kovacheva, D.; Chakraborty, A.; Kravchuk, T.; Ravikumar, R.; Talianker, M.; Grinblat, J.; Burstein, L.; Kauffmann, Y.; Major, D. T.; Markovsky, B.; Aurbach, D., Improving Performance of $\text{LiNi}_{0.8}\text{Co}_{0.1}\text{Mn}_{0.1}\text{O}_2$ Cathode Materials for Lithium-Ion Batteries by Doping with Molybdenum-Ions: Theoretical and Experimental Studies. *ACS Applied Energy Materials* **2019**, *2* (6), 4521-4534.
- .64 Grimme, S., Accurate description of van der Waals complexes by density functional theory including empirical corrections. *Journal of Computational Chemistry* **2004**, *25* (12), 1463-1473.

- .65 Maintz, S.; Deringer, V. L.; Tchougréeff, A. L.; Dronskowski, R., LOBSTER :A tool to extract chemical bonding from plane-wave based DFT. *Journal of Computational Chemistry* **2016**, 37 (11), 1030-1035.
- .66 Maintz, S.; Deringer, V. L.; Tchougréeff, A. L.; Dronskowski, R., Analytic projection from plane-wave and PAW wavefunctions and application to chemical-bonding analysis in solids. *Journal of Computational Chemistry* **2013**, 34 (29), 2557-2567.
- .67 Dronskowski, R.; Bloechl, P. E., Crystal orbital Hamilton populations (COHP): energy-resolved visualization of chemical bonding in solids based on density-functional calculations. *The Journal of Physical Chemistry* **1993**, 97 (33), 8617-8624.
- .68 Deringer, V. L.; Tchougréeff, A. L.; Dronskowski, R., Crystal Orbital Hamilton Population (COHP) Analysis As Projected from Plane-Wave Basis Sets .*The Journal of Physical Chemistry A* **2011**, 115 (21), 5461-5466.
- .69 Urban, A.; Seo, D.-H.; Ceder, G., Computational understanding of Li-ion batteries. *npj Computational Materials* **2016**, 2 (1), 16002.
- .70 Islam, M. S.; Fisher, C. A. J., Lithium and sodium battery cathode materials: computational insights into voltage, diffusion and nanostructural properties. *Chemical Society Reviews* **2014**, 43 (1), 185-204.
- .71 Chakraborty, A.; Kunnikuruvan, S.; Kumar, S.; Markovsky, B.; Aurbach, D.; Dixit, M.; Major, D .T., Layered Cathode Materials for Lithium-Ion Batteries: Review of Computational Studies on $\text{LiNi}_{1-x-y}\text{Co}_x\text{Mn}_y\text{O}_2$ and $\text{LiNi}_{1-x-y}\text{Co}_x\text{Al}_y\text{O}_2$. *Chemistry of Materials* **2020**, 32 (3), 915-952.
- .72 Ebadi, M.; Brandell, D.; Araujo, C. M., Electrolyte decomposition on Li-metal surfaces from first-principles theory. *The Journal of Chemical Physics* **2016**, 145.(20)
- .73 Kamphaus, E. P.; Angarita-Gomez, S.; Qin, X.; Shao, M.; Engelhard, M.; Mueller, K. T.; Murugesan, V.; Balbuena, P. B., Role of Inorganic Surface Layer on Solid Electrolyte Interphase Evolution at Li-Metal Anodes. *ACS Applied Materials & Interfaces* **2019**, 11 (34), 31467-31476.
- .74 Zhao, S.; Zhang, Y.; Weber, W. J., Ab Initio Study of Electronic Excitation Effects on SrTiO_3 . *The Journal of Physical Chemistry C* **2017**, 121 (48), 26622-26628.
- .75 Chakraborty, T.; Hens, A.; Kulashrestha, S.; Chandra Murmu, N.; Banerjee, P., Calculation of diffusion coefficient of long chain molecules using molecular dynamics. *Physica E: Low-dimensional Systems and Nanostructures* **2015**, 69, 371-377.
- .76 Galvez-Aranda, D. E.; Seminario, J. M., Ab Initio Study of the Interface of the Solid-State Electrolyte $\text{Li}_9\text{N}_2\text{Cl}_3$ with a Li-Metal Electrode. *Journal of The Electrochemical Society* **2019**, 166 (10), A2048.
- .77 Martínez, L.; Andrade, R.; Birgin, E. G.; Martínez, J. M., PACKMOL: A package for building initial configurations for molecular dynamics simulations. *Journal of Computational Chemistry* **2009**, 30 (13), 2157-2164.
- .78 Bano, A.; Major, D. T., Coexistence of Rashba effect and spin–valley coupling in TiX_2 (X = Te, S, and Se) based heterostructures. *Applied Physics Letters* **2023**, 122.(18)
- .79 Lu, Y.; Chen, J.; Coupin, M. J.; Sinha, S.; Warner, J. H., Lattice-Mismatch-Driven Small-Angle Moiré Twists in Epitaxially Grown 2D Vertical Layered Heterostructures. *Advanced Materials* **2022**, 34 (43), 2205403.
- .80 Chen, P.; Chan, Y. H.; Fang, X. Y.; Zhang, Y.; Chou, M. Y.; Mo, S. K.; Hussain, Z.; Fedorov, A. V.; Chiang, T. C., Charge density wave transition in single-layer titanium diselenide. *Nature Communications* **2015**, 6 (1), 8943.
- .81 Zhang, R.; Wang, C.; Zou, P.; Lin, R.; Ma, L.; Yin, L.; Li, T.; Xu, W.; Jia, H.; Li, Q.; Sainio, S.; Kisslinger, K.; Trask, S. E.; Ehrlich, S. N.; Yang, Y.; Kiss, A. M.; Ge, M .;Polzin, B. J.; Lee, S. J.; Xu, W.; Ren, Y.; Xin, H. L., Compositionally complex doping for zero-strain zero-cobalt layered cathodes. *Nature* **2022**, 610 (7930), 67-73.

- .82 Sun, H. H.; Kim, U.-H.; Park, J.-H.; Park, S.-W.; Seo, D.-H.; Heller, A.; Mullins, C. B.; Yoon, C. S.; Sun, Y.-K., Transition metal-doped Ni-rich layered cathode materials for durable Li-ion batteries. *Nature Communications* **2021**, *12* (1), 6552.
- .83 Susai, F. A.; Bano, A.; Maiti, S.; Grinblat, J.; Chakraborty, A.; Sclar, H.; Kravchuk, T.; Kondrakov, A.; Tkachev, M.; Talianker, M.; Major, D. T.; Markovsky, B.; Aurbach, D., Stabilizing Ni-rich high energy cathodes for advanced lithium-ion batteries: the case of $\text{LiNi}_{0.9}\text{Co}_{0.1}\text{O}_2$. *Journal of Materials Chemistry A* **2023**, *11*, 12958-12972, (24)
- .84 Dixit, M.; Markovsky, B.; Aurbach, D.; Major, D. T., Unraveling the Effects of Al Doping on the Electrochemical Properties of $\text{LiNi}_{0.5}\text{Co}_{0.2}\text{Mn}_{0.3}\text{O}_2$ Using First Principles. *Journal of The Electrochemical Society* **2017**, *164* (1), A6359.
- .85 Wen, L.; Shi, J.; Zhang, Q.; Wang, F.; Wang, S.; Zhang, S.; Wang, Q.; Mao, K.; Long, F.; Gao, Y., $\text{Ti}_3\text{C}_2\text{T}_x\text{-TiSe}_2$ analogous heterostructure for flexible zinc ion battery. *Journal of Materials Science & Technology* **2023**, *150*, 225-232.
- .86 Zhang, Z.; Yuan, X.; Peng, Y.; Zhao, S.; Zhou, N., First-principles calculations study of $\text{TiS}_2/\text{Ti}_2\text{CS}_2$ heterostructure as an anode material for Li/Na/K-ion batteries. *Computational Materials Science* **2022**, *215*, 111784.
- .87 K. Nair, A.; Da Silva, C. M.; Amon, C. H., Enhanced Alkali-Ion Adsorption in Strongly Bonded Two-Dimensional $\text{TiS}_2/\text{MoS}_2$ van der Waals Heterostructures. *The Journal of Physical Chemistry C* **2023**, *127* (20), 9541-9553.
- .88 Thinius, S.; Islam, M. M.; Heitjans, P.; Bredow, T., Theoretical Study of Li Migration in Lithium-Graphite Intercalation Compounds with Dispersion-Corrected DFT Methods. *The Journal of Physical Chemistry C* **2014**, *118* (5), 2273-2280.
- .89 Yuan, X.; Chen, Z.; Huang, B.; He, Y.; Zhou, N., Potential Applications of $\text{MoS}_2/\text{M}_2\text{CS}_2$ ($\text{M} = \text{Ti}, \text{V}$) Heterostructures as Anode Materials for Metal-Ion Batteries. *The Journal of Physical Chemistry C* **2021**, *125* (19), 10226-10234.
- .90 Bafekry, A.; Naseri, M.; Faraji, M.; Fadlallah, M. M.; Hoat, D. M.; Jappor, H. R.; Ghergherehchi, M.; Gogova, D.; Afarideh, H., Theoretical prediction of two-dimensional BC_2X ($\text{X} = \text{N}, \text{P}, \text{As}$) monolayers: ab initio investigations. *Scientific Reports* **2022**, *12* (1), 22269.
- .91 Singh, M.; Chakraborty, B., 2D BN-biphenylene: structure stability and properties tenability from a DFT perspective. *Physical Chemistry Chemical Physics* **2023**, *25* (23), 16018-16029.
- .92 Yamijala, S. S. R. K. C.; Ali, Z. A.; Wong, B. M., Acceleration vs Accuracy: Influence of Basis Set Quality on the Mechanism and Dynamics Predicted by Ab Initio Molecular Dynamics. *The Journal of Physical Chemistry C* **2019**, *123* (41), 25113-25120.
- .93 Luo, Z.; Burrows, S. A.; Smoukov, S. K.; Fan, X.; Boek, E. S., Extension of the TraPPE Force Field for Battery Electrolyte Solvents. *The Journal of Physical Chemistry B* **2023**, *127* (10), 2224-2236.

Supplementary Information

Atomistic Modelling of High-Entropy Layered Anodes and Their Electrolyte Interface

Amreen Bano* and Dan T Major

Department of Chemistry and Institute of Nanotechnology and Advanced Materials,
Bar-Ilan University, Ramat Gan, Israel-5290002

*Email: banoamreen.7@gmail.com

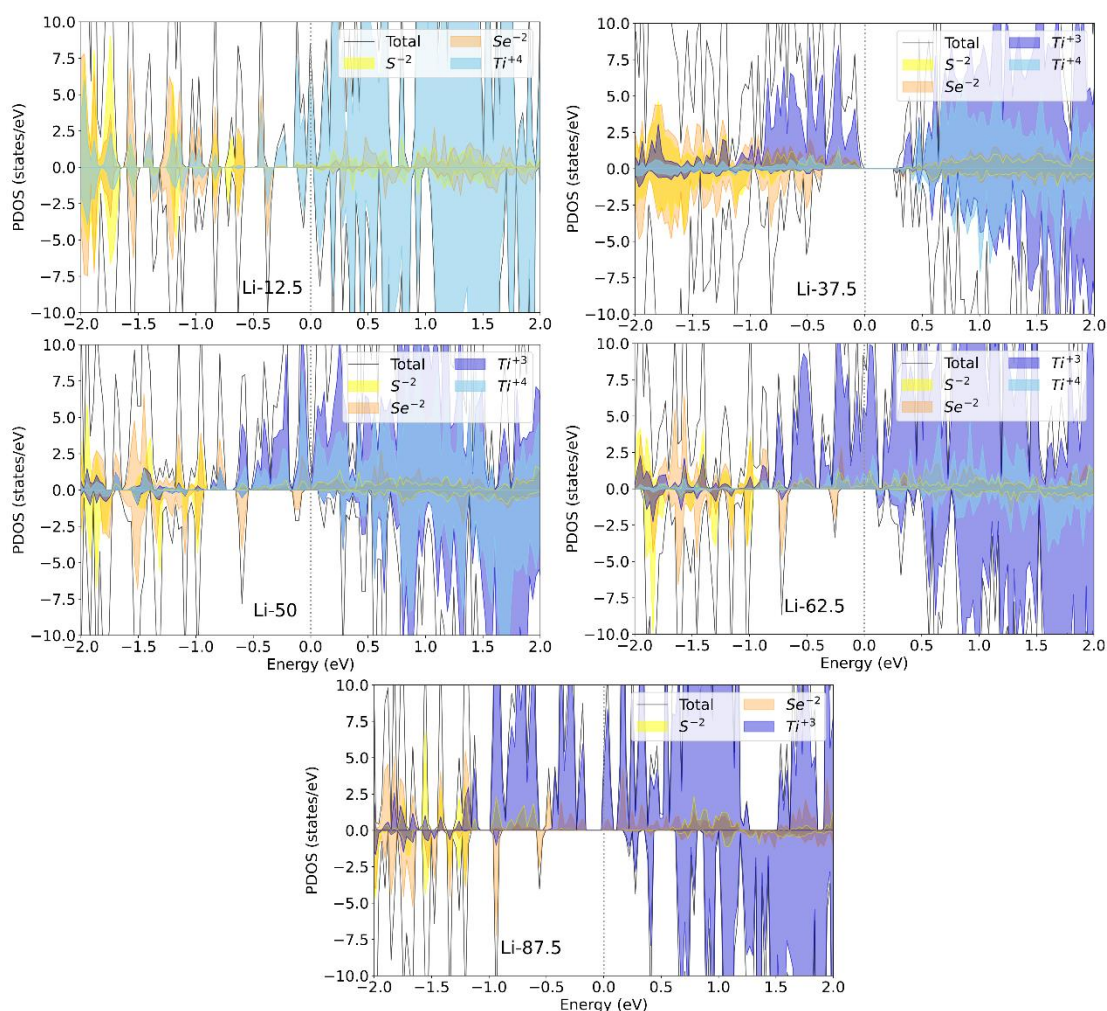


Figure S1: Partial density of states (PDOS) of TSS-HS at different Li-concentration levels showing change in electronic states of constituent elements of the layered anode material. The dotted line indicates that the Fermi level was set at 0.0 eV.

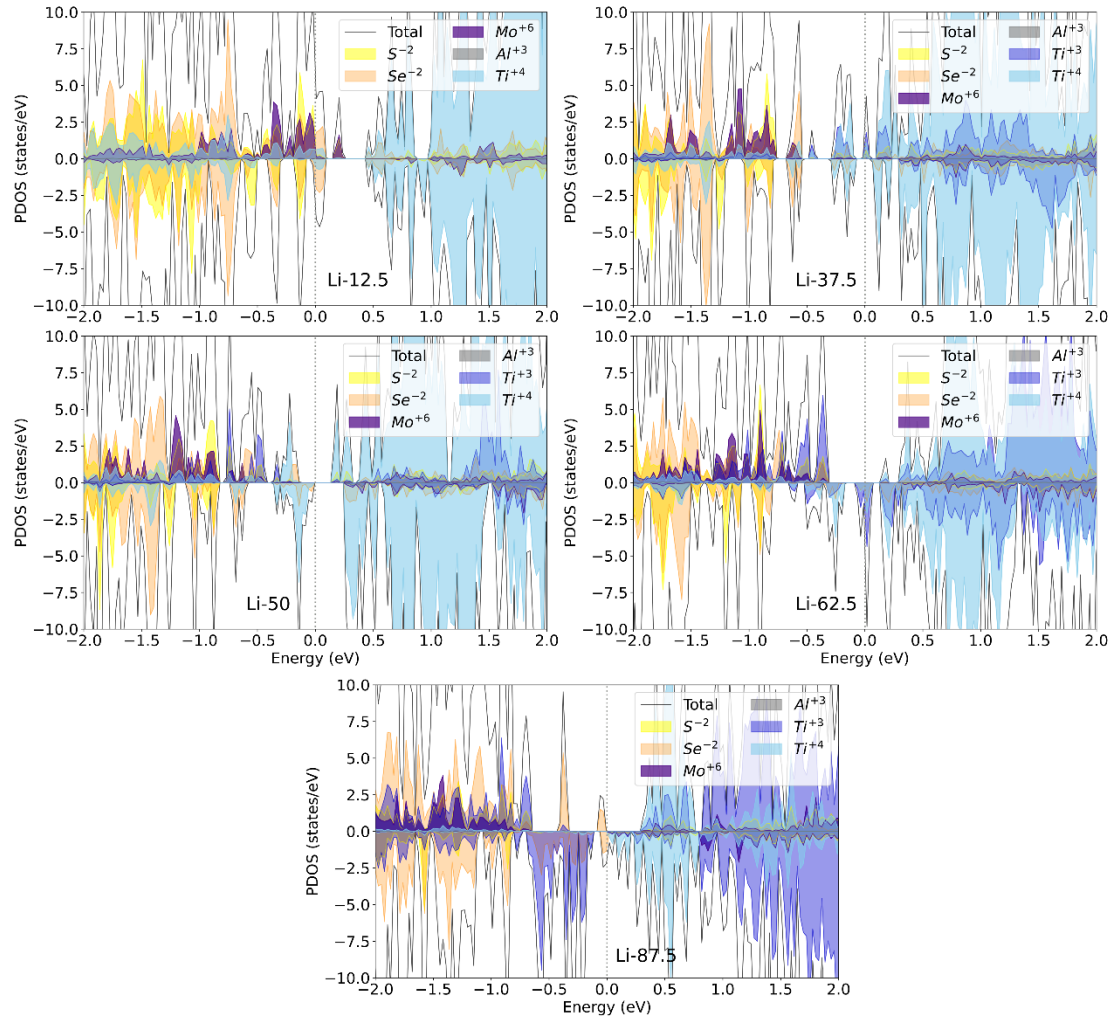


Figure S2: Partial density of states (PDOS) of TSS-HE at different Li-concentration levels showing change in electronic states of constituent elements of the high entropy anode material. The dotted line indicates that the Fermi level was set at 0.0 eV.